Heaps of sand in flows within a split-bottom Couette cell

Miguel Cabrera ●* and Oscar Polanía ●

Department of Civil and Environmental Engineering, Universidad de los Andes, Bogotá, Colombia

In this paper, we study the flow of angular grains in a split-bottom Couette cell. Grains departing from a spherical shape result in collective flow fields that form a heap on the free surface. Here we extend on previous observations in split-bottom cells, exploring a wider range of flows within the inertial regime and finding a richness collection of behaviours. Surface height profiles and velocity profiles are accurately measured with digital image analysis. These measurements allow the characterization of the flow regimes within the cell and the heap morphology. We show that the known flow regimes in split-bottom geometries, like the universal and wall-collapsed regimes, can also be observed in moderately high inertial flows, extending the range for studying universal shear banding. The heap morphology is amplified by the flow inertia, with a partial collapse when the cell comes to a halt. Moreover, at high angular velocities, flows under low confinement will spread radially outwards, while flows under high confinement will develop localized particle ejections. Our results complement the observation of free-surface deformations of flows of nonspherical grains. These observations suggest a need for considering deformable free surface boundary conditions in the simulation of angular grains during shear, with repercussions in the characterization and prediction of natural mass flows.

I. INTRODUCTION

Granular flows are found across scales, from geophysical mass flows, e.g., landslides, debris flows, pyroclastic flows, and snow avalanches, to industrial processes, e.g., pharmaceutical, food, and construction industries. The accurate description of granular media under shear is of particular relevance, both for predicting a mobilized volume and for describing its motion. Granular media exhibit a complex mechanical behavior as a function of local properties like its grain size, grain shape, and density, as well as a function of its interaction with the ambient fluid [1–6]. Moreover, granular media behave as a collective system, transitioning between localized dense and loose assemblies [7,8]. On it, volume fraction and shear rate allows the distinction of three main flow regimes, a quasistatic, an inertial, and a gaseous regime, describing the mechanical behavior as a solidlike, a fluidlike, and a gaslike medium, respectively [9].

In this work we explore the collective behavior of angular grains under continuous shear, characterizing the emergent features that result from grain shape and shear intensity. A granular medium under shear develops a localized discontinuity in the velocity gradient. This discontinuity is called a shear band and in the quasistatic regime is commonly theorized to be up to a few grains wide [10–12]. Recent works show that with the use of a split-bottom cell it is possible to widen the shear band, while isolating the granular media from the cell boundaries [13–17]. Wide shear bands provide a smoother transition between the moving and static regions.

This characteristic allows the description of shear bands in a continuum framework and sets a benchmark for the study of nonlocal effects for flows transitioning across the aforementioned regimes [18].

A split-bottom cell consists of two concentric basal rings, one rotating and one fixed, shearing a granular material within a cylindrical container [12]. A cylinder, moving synchronously with the inner ring, can be added to this setup, resulting in a split-bottom Couette cell (see Fig. 1) [13–16,19]. In a split-bottom cell, the shear band localizes at the transition between the rotating and fixed basal rings and its ascent is controlled by the amount of material within the cell and the rotation speed [13–15].

Previous studies in split-bottom cells explored the transition from a quasistatic to slow inertial flow regimes, highlighting the independence of the shear band width (W) with the split radius (R_s) and its dependence with the grain size and the grain shape [13]. Grain shape can be described as a function of grain roundness and grain symmetry, also known as sphericity [20]. Roundness (R) is defined as the ratio between the average grain corner radii and the grain inscribed radius, and sphericity (S) is defined as the ratio between grain length and grain width. The combination of these two aspect ratios result in either spherical or slender grains and either round or angular grains.

The effect of grain shape has been studied in split-bottom cells, focusing on slender particles (e.g., oblate, prolate) and showing an interesting outcome on the deformation of the initially flat free-surface in the form of heaps [16,21,22]. In these studies the heap emerges from the collective action of particle alignment in the shear band vicinity and from a secondary convective flow in a plane normal to the direction of rotation [21].
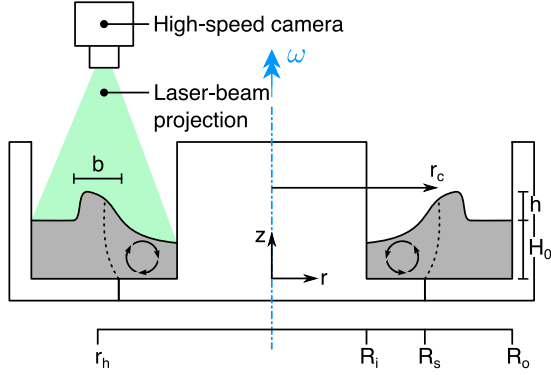
---

*ma.cabrera140@uniandes.edu.co

FIG. 1. Schematic of the split-bottom Couette cell, creating a shear band (dotted line) within the granular medium (gray shaded volume) and resulting in an alteration of the free surface in the form of a heap. The heap has height h, width b, and center r_h. A laser beam projects onto the material surface, while a high-speed camera records the material movement and laser deflection.

The lack of a dominant orientation at the grain scale is theorized to explain the absence of heaps in experiments with spherical or nearly spherical beads [21]. Despite the clear understanding of these processes in split-bottom cells, these observations remain to be confirmed in flows with angular grains and under higher inertial regimes. Angular grains are found to increase the granular medium shear strength and reduce its packing fraction [2,23]. Moreover, the shape effects of angular grains can shed light on the kinematics of natural flows, where a similar heaping process is observed in the formation of lateral levees [24–27].

In this paper we study the flow of angular grains in a split-bottom Couette cell. We aim to extend the current set of observations on heaps in split-bottom cells, spanning the transition from slow to highly inertial flows. These observations allow the identification of a wider range of flow regimes in a split-bottom cell, transitioning from moderate to highly inertial flows. The paper is organized as follows. The experimental setup, materials, and experimental protocol are presented in Sec. II. The shear zone characteristics are discussed in Sec. III. In Sec. IV we quantitatively study the heap morphology, during and after shear, and describe the limit behaviours under high rotation speeds. Finally, the summary and conclusions are presented in Sec. V.

II. SPLIT-BOTTOM COUETTE CELL

The split-bottom Couette cell in this work consists of a stationary outer cylinder of radius $R_o = 165$ mm, an inner rotating cylinder of radius $R_i = 65$ mm, and an inner rotating split-bottom of radius $R_s = 105$ mm (see Fig. 1).

The inner cylinder and inner split-bottom rotates at an angular velocity ω, controlled by a two-phase hybrid step motor with a holding torque of 0.18 N m. The volume between the inner and outer cylinders is adjusted with a filling height H_0. During shear, the innermost radial location of the granular medium r_i is equal to R_i in most cases and $r_i > R_i$ when the granular material detaches from the inner cylinder.

Moreover, sandpaper grade N60 is glued to the rotating parts, providing rough moving boundaries. Note that in this setup, shear is driven from the inner cylinder, opposite to previous works where shear is driven from the outer cylinder.

Dimensional analysis provides an useful tool for describing the kinematics of granular materials as a ratio between the local grains inertia and the global level of confinement [28]. A common dimensionless quantity for this description is the inertial number ($I = \dot{\gamma}d/\sqrt{P/\rho}$) [9], where d and ρ are the mean particle diameter and particle density, respectively, and $\dot{\gamma}$ and P are the flow shear rate and confining pressure, respectively. In a split-bottom cell geometry, the imposed rotation generates a characteristic shear rate in the radial direction in the form of $\dot{\gamma} = u_\theta/R_s = \omega$, assuming $u_\theta = \omega R_s$. Gravity (g) acts in the transverse direction z, resulting in a geostatic pressure $P = \rho g H_0$, with a uniform distribution in the plane normal to z and assuming negligible centrifugal effects. Under these considerations, the definition of the inertial number is

$$I = \frac{\omega d}{\sqrt{gH_0}}. \tag{1}$$

Centrifugal effects are not considered in the computation of I as its contribution to the confining pressure is minimal and becomes only dominant when generating flow instabilities as those presented in Sec. IV B. An alternative for its inclusion is adding the term $\omega^2 R_s^2$ in the computation of the confining pressure P.

The magnitude of I allows the distinction between a regime governed by long-lasting contacts (quasistatic regime for low values of I) and a regime where the macroscopic friction depends on the shear rate (inertial regime for high values of I).

Previous studies in split-bottom geometries had explored these regimes, focusing on the range between 0.0002 and 0.0149 for the study of shear bands in granular flows [13–15,19], and reaching up to $I = 0,4825$ for the study of rate-independent convective flows without static regions in Ref. [29]. This richness of behaviours in a split-bottom cell encourages the study of a wider range of inertial flows, transitioning from well established flow regimes towards the appearance of rate-independent flows at high inertial numbers. As a result, in this paper we study flows within the inertial regime in the range of $I = [0.002–0.119]$. This range is explored by varying the filling height and the angular velocity in the range of $H_0 = [10–74]$ mm and $\omega = [0.88–21.4]$ rad/s, respectively.

Experiments are performed with crushed sand of mean particle diameter $d = 1.77$ mm and particle density $\rho = 2400$ kg/m³. The sand presents an angle of internal friction $\varphi = 40.0°$, measured in geotechnical direct shear tests. Sand sphericity and roundness are assessed by analyzing 2D digital images of single grains [20,30,31], resulting in the following shape parameters: $S = 0.82 \pm 0.11$ and $R = 0.32 \pm 0.10$ [see Figs. 2(d)–2(i)].

Note that a sphere has shape factors $[S, R] = [1, 1]$, a cube has shape factors $[S, R] = [1, 0]$, while boulders in geophysical mass flows are catalogued as spherical and angular with shape factors $[S, R] \approx [0.72, 0.21]$ [32]. By using crushed sand we aim at exploring an equivalent response of grain
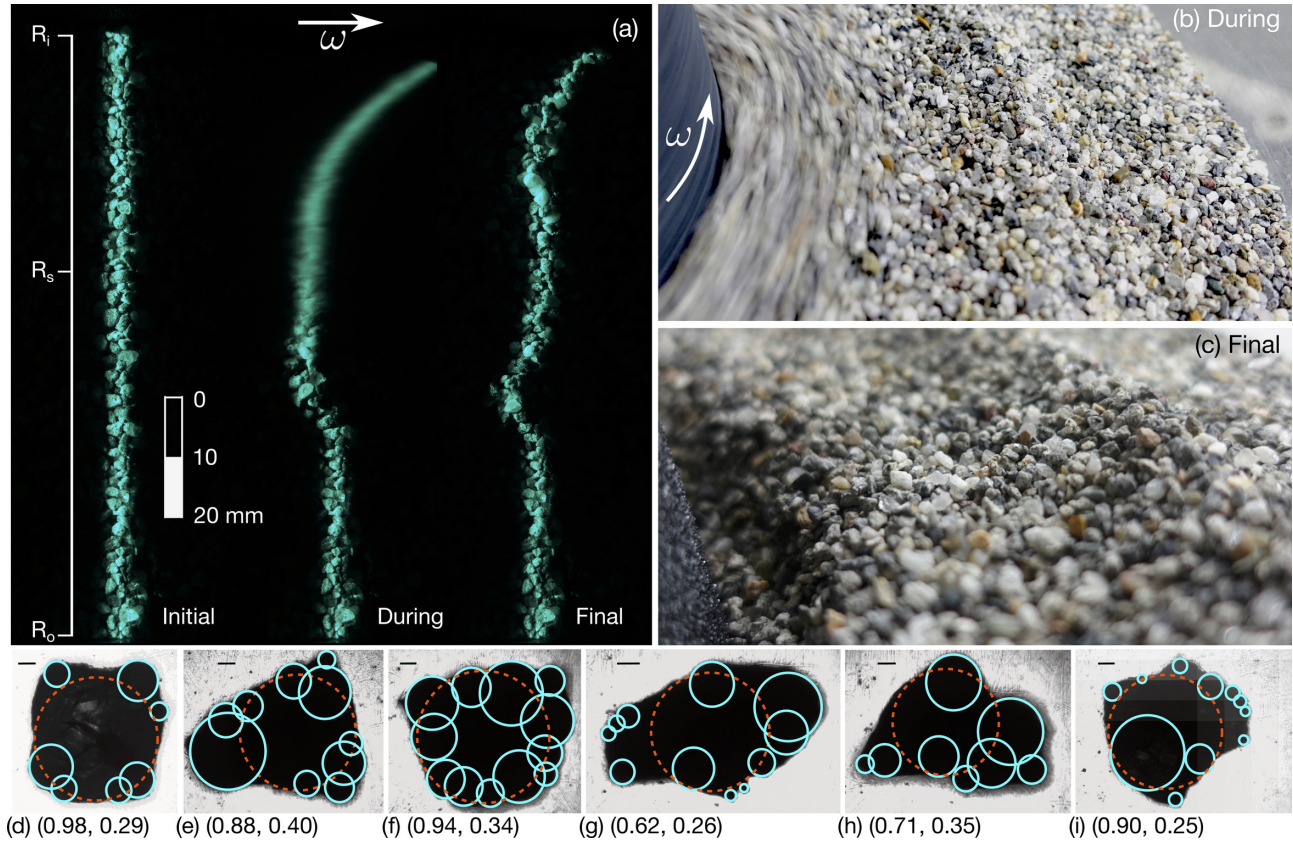
FIG. 2. (a)–(c) Snapshots of a sand flow within a split-bottom Couette cell, with initial height $H_0 = 30$ mm and $\omega = 12.57$ rad/s ($I = 0.041$). (a) Laser projections before, during and after shear; and close up views, (b) during, and (c) after shear. (d)–(i) Photographs of sand grains with their respective sphericity and roundness (S, R) measurements. The dashed inscribed circle is used in the calculation of S, and the continuous circles mark the grains' corner radii employed in the calculation of R. The horizontal scale bar corresponds to a distance of 100 μm.

shape effects as those observed in natural materials, like soils and rocks [30,33].

A test starts by filling the cell with sand up to H_0 and leveling its surface with a rigid plate. At initiation, the inner cylinder rotates at a constant acceleration until reaching the desired ω. Experiments are performed for 100 rotations. A laser beam projects onto the flow surface at an azimuthal angle between $43°$ to $48°$, and a high-speed camera records from a zenithal location a region of interest (ROI) at a frame rate of 480 Hz (see Fig. 1). The recorded images are employed for two measurements, the flow surface profile and the surface velocity field.

The surface profile is estimated from the laser projection along a radial axis, computing the line deflection before, during and after test [see Fig. 2(a)]. The surface velocity field is measured by means of particle image velocimetry [34], computing the tangential (u_θ) and radial (u_r) velocity components within the ROI. As friction during test wears down both grains and the roughened layer, the sand grains and sandpaper cover are changed every seven tests.

III. SHEAR ZONE CHARACTERIZATION

After initiation, the rotating parts shear the granular material, generating a moving annulus of sand [14,16,35]. As a

result of shear, the initially flat surface deforms, developing a heap that remains after the apparatus comes to a halt. Figure 2 shows the change in the laser beam projection onto the sand surface before, during and after shear, and close-up views of the sand heap during and after shear. The heap locates between the volume of moving grains and the volume of stagnant grains.

Figure 3 presents the height and velocity profiles extracted from the image analysis of a typical test ($H_0 = 30$ mm, $\omega = 8.48$ rad/s). These measurements correspond to an average measurement of 100 rotations during shear, resulting in minimal variability and being confirmed by the reproducibility of experiments. These profiles allow the characterization of the flow surface as a function of H_0 and ω [14,15,35].

The heap forms over a wide diluted area during shear [16] and part of it collapses after shearing ceases. The after-shear heap preserves a narrow peak with height h, while spreading and filling radially inwards. Moreover, the velocity profile during shear presents a predominant motion in the tangential direction ($u_\theta \gg u_r$), decreasing along the r axis [see Fig. 3(b)].

The velocity profile allows the distinction of a moving zone ($u_\theta > 0$) and a stagnant zone ($u_\theta \approx 0$), providing secondary information to link with the height profile. Previous studies characterize the moving zone in terms of the shear band width
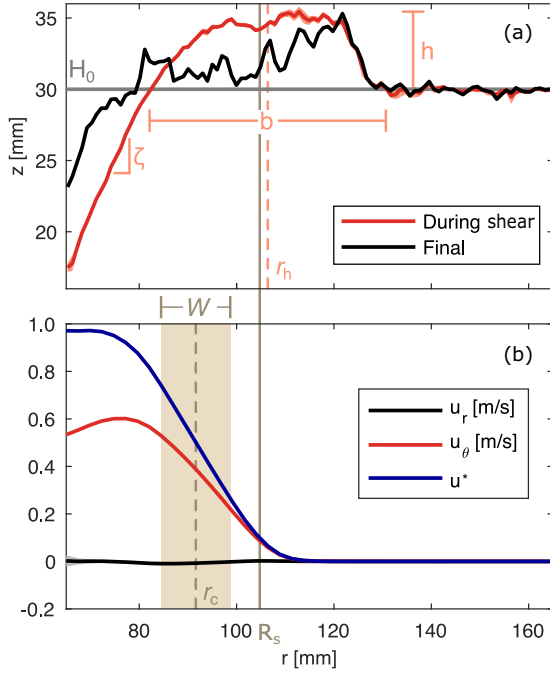
FIG. 3. (a) Height and (b) velocity profiles for a sand flow with initial height $H_0 = 30\,\text{mm}$ and $\omega = 8.48\,\text{rad/s}$ ($I = 0.085$). The shaded region in (b) indicates the shear band width W and its middle coordinate r_c. The continuous line crossing both plots refers to the split bottom radius R_s. All profiles show a shaded region with the measurement standard deviation.

(W) and shear band center (r_c), obtaining W and r_c by fitting the normalized velocity profile $u^* = u_\theta/(\omega r)$ to a Gaussian function [14,15,19]. In this study, we measured r_c relative to u^*, identifying r_c as the median location in the range between $du^*/dr < 0$ [see Fig. 3(b)].

Studies of flows in a split-bottom cell have found that the shear band location r_c depends only on H_0 and R_s, but not on the local properties of the granular media nor on the shear rate [14,36]. This relation is expressed as

$$\frac{r_c}{R_s} = 1 - \left(\frac{H_0}{R_s}\right)^{2.5}. \tag{2}$$

The dependency of r_c on H_0 and R_s is confirmed for flows at low inertial numbers ($I < 10^{-2}$), but as the system inertia grows, r_c falls off the trend, approaching towards the center and indicating a separate behavior at moderately high inertial numbers, low filling heights, and with angular grains (see Fig. 4). At moderately high inertial flows, the occurrence of significant vertical motion within the shear band departs from the traditional assumptions for flows in split-bottom cells [14,36]. Moreover, at moderately high inertial numbers, the role of the centrifugal acceleration term is clearly non-negligible and the simplification of the moving annulus into a flat and horizontal surface might become significant. Following the work of Unger et al. [36] and Jop [37], it is possible to argue that the shear band position, closer to the center for $I > 10^{-2}$, might be driven by a decrease in the lateral pressure, caused by an increase in the centrifugal acceleration, that results in the decrease of the shear rate that lowers the
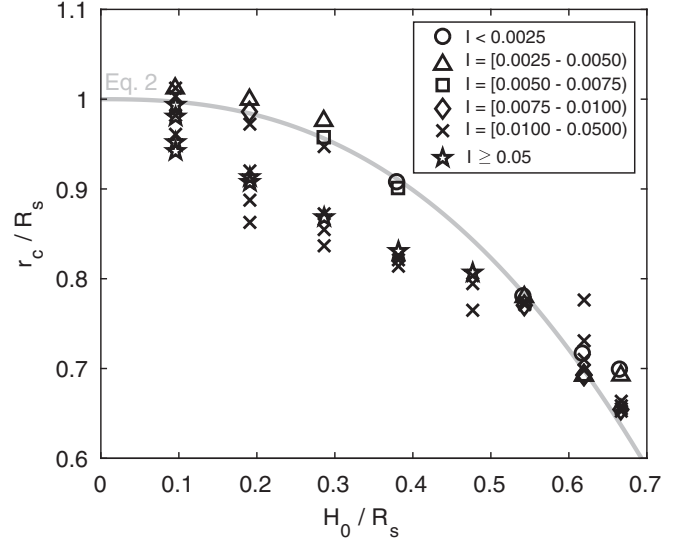

FIG. 4. Surface shear band location r_c as a function of filling height (H_0) and split-bottom radius (R_s). The continuous line is the empirical fit shown in Eq. (2) which describes flows at low inertial numbers ($I < 0.01$) [14,36].

effective friction coefficient locally. The study of centrifugal effects, within the granular flow falls outside the scope of the current work, but its development is more than encouraging in understanding this behavior.

Fenistein et al. (2004) distinguished two flow regimes within the split-bottom cell, an universal regime and a wall-collapsed regime [14]. In the universal regime, the shear band is not in contact with the cell boundaries, the velocity profile $u_\theta(r)$ has a maximum between (R_i, R_s) (see inset in Fig. 5), and the dimensionless velocity profile $u^*(\lambda)$ follows a master error function in the form of

$$u^* = 1 - \left[\tfrac{1}{2} + \tfrac{1}{2}\text{erf}(\lambda)\right], \tag{3}$$

where $\lambda = (r - r_c)/W$ is a scaled radial axis that collapses all profiles within the universal regime into a single curve. In the wall-collapsed regime, the shear band is in contact with the rotating inner cylinder and both velocity profiles, $u_\theta(r)$ and $u^*(r)$, decrease exponentially with r [15].

Figure 5 presents the collapse of all dimensionless velocity profiles within the universal and wall-collapsed regimes. In addition to the experiments with sand, some experiments are performed with spherical glass beads, of $d = 2.0\,\text{mm}$ and $\rho_p = 2500\,\text{kg/m}^3$ (hollow markers and dashed lines in Fig. 5), allowing a direct comparison of the shear band observations in the universal regime. As reported by Schall and van Hecke, the relationship between the shear band location and its dimensions is independent of the grain shape [12], collapsing onto the error function in Eq. (3). These results provide an indication that the universal regime in a split-bottom Couette cell holds consistently for moderately high inertial numbers ($0.01 \leqslant I \leqslant 0.05$), extending the range for studying universal shear banding outside the quasistatic flow regime. The range for moderately high inertial flows is extracted from flows that do not collapse in Eq. (2) ($I > 0.01$) and that do not develop radial spread ($I < 0.05$).
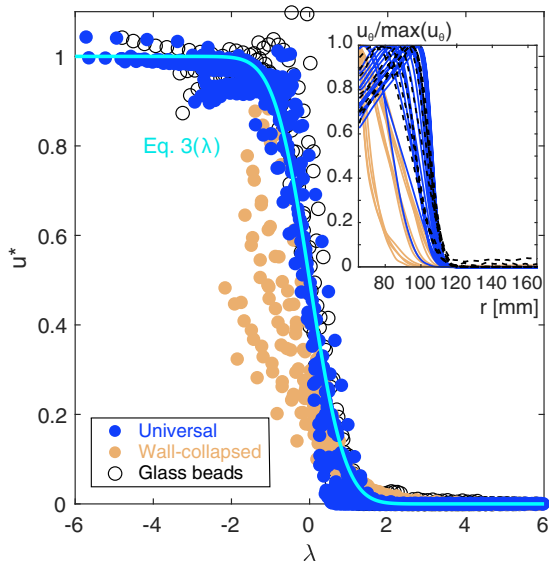
FIG. 5. Normalized velocity profiles $u^*(\lambda)$ for flows within the universal and wall-collapsed regimes. Inset: Velocity profiles as a function of r. The flow profiles transition from a Gaussian bulk shear zone described by Eq. (3), to an exponential wall-localized shear band [15]. The dashed line in the inset corresponds to the velocity profiles of glass beads. Note that the split-bottom base has a radius $R_s = 105$ mm.

The range of H_0 and ω explored in this work provides a richness set of behaviors to be explored in split-bottom cells. Figure 6 presents the phase diagram from the explored domain as a function of H_0 and ω, highlighting the location of the universal and wall-collapsed regimes, and introduce two observed instabilities at high angular velocities. These instabilities result in the radial spread of the moving annulus and in the ejection of particles at its interaction with the inner cylinder.

For more details, the Appendix summarizes the measurements performed on the shear band and heap during shear.

Flows in the universal regime are consistently faster than flows in the wall-collapsed regime, both being faster by decreasing H_0. This observation hints to a relation between the
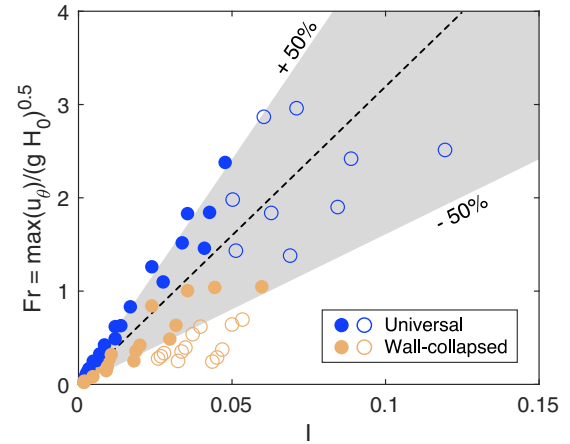

FIG. 7. Variation of the Froude number Fr as a function of the inertial number I. The dashed line presents a trend in the form of Fr = aI for all tests without instabilities, with $a = 32.2$, and the dashed region marks a $\pm 50\%$ deviation from this ratio. Hollow markers indicate tests where instabilities were observed.

moving annulus velocity and its self-weight. The ratio between the grain speed propagation and the gravity wave speed can be approximated by the Froude number, defined from the surface velocity profiles as Fr = $\max(u_\theta)/(gH_0)^{0.5}$.

For similar levels of inertia, the Froude number is always higher in the universal regime than in the wall-collapsed regime. This increased velocity in the universal regime results from a lesser resistance, associated with the granular medium self-weight and the undisturbed shear band, favoring the motion of the moving granular annulus. A linear trend between Fr and I is expected, following a form of Fr = aI, with $a = 32.2$ as a fitting term for all tests in the universal and wall-collapsed regimes. The resultant trend confirms the separation between flow regimes within a $\pm 50\%$ deviation. Regarding the observed instabilities, tests with radial spread fall consistently outside the $\pm 50\%$ deviation, but flows with particle ejection do fall within, indicating that the latter is a local instability occurring at the grain scale while the former effects globally the flow. Moreover, the instabilities in Fig. 7 are well distinguished, resulting in radial spread at Fr > 1
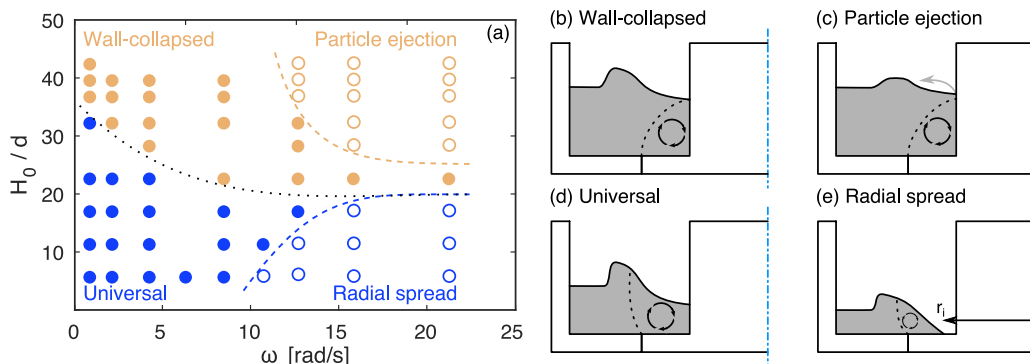
FIG. 6. Phase diagram for sand flows in a split-bottom Couette cell as a function of the angular velocity ω and filling height H_0 normalized by the grain diameter d. The tests here presented correspond to nearly monodisperse systems. Aside from the effects of H_0/d on the flow regime within the cell [e.g., (b) wall-collapsed, (d) universal], two instabilities are observed at high rotational velocities [e.g., (c) particle ejection, (e) radial spread]. The instabilities (c and d) are discussed in Sec. IV B.

and particle ejection at Fr < 1. This differentiation allows the interpretation that under extreme levels of inertia, the moving granular annulus would lead to the development of specific flow processes, whether the conditions are of subcritical or supercritical flows.

IV. HEAP CHARACTERIZATION

In this work, granular heaps are observed in all experiments, regardless of the flow regime in the split-bottom cell. In this section, we present a detailed description of the influence of H_0 and ω on the heap morphology. First, we explore the effect of shear on the heap configuration and its partial collapse when shear is ceased. Second, we study the instabilities reached at high angular velocities.

A. Heap configuration

The mechanism leading to heap formation in a split-bottom cell is described by Wortel *et al.* and Fischer *et al.* as the collective action of primary and secondary flow fields [21,22]. In the primary flow field, the grains reorient and dilate within the shear band, establishing a steady and radially varying packing in the sheared granular medium. In the secondary flow field, a convective flow, normal to the tangential velocity u_θ, uplifts the grains near the shear band, moves them towards the rotation axis, then sinks them towards the rotating base, and finally moves them radially outwards closing the loop [38]. The convective flow is driven by the combination of shear-induced dilation and self-weight [39]. A verification of this convective cell can be observed by the radial motion on the surface, which consistently points inwards in all tests. A result of this secondary flow leads to a depression around the inner cylinder and an accumulation of grains at the shear band outer region. As the system rapidly reaches a collective steady flow rate, the heap formation and its geometry are independent of the initial granular packing and of the initial grain orientation [21].

During shear, the heap forms on a wide region consisting of all points above H_0. The heap is described with a peak height h, basal width b, and centered at r_h (see Figs. 1 and 3). The heap forms and grows radially outwards until reaching h. The heap distributes uniformly along the split-bottom cell with a cylindrical symmetry, but without preserving a symmetric cross section in the (r, z) plane. Figure 8 presents the variation of the heap configuration variables (h, b, r_h) as a function of H_0 and ω, represented by the inertial number I. The distinction between flow regimes is kept for simplicity, and the hollow markers represent experiments with flow instabilities.

The heap height h increases with I, resulting in higher heaps for flows in the wall-collapsed regime and reaching over a greater relative thickness (h/H_0) in flows in the universal regime [see Figs. 8(a) and 8(b)]. Overall, flows in the universal and wall-collapsed regimes result in heaps where h hardly exceeds $H_0/2$ or a maximum thickness of $5d$, indicating a limiting state above which the heap becomes unstable and collapses during shear.

It is possible to well distinguish the flow regime with b. Note that most flows within the universal regime result in
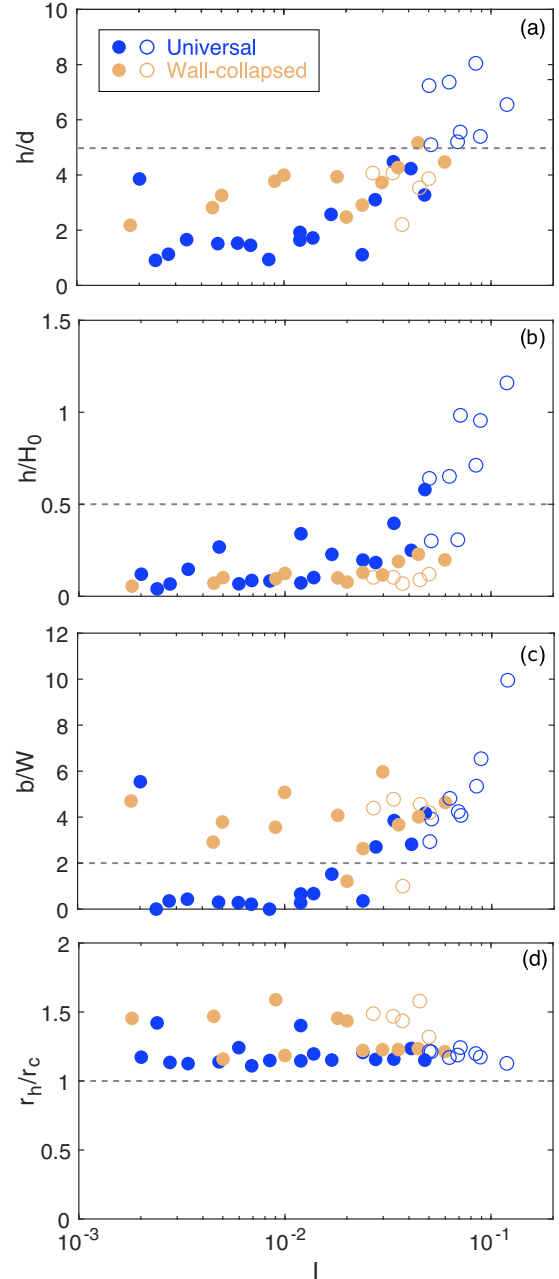

FIG. 8. Variation of heap configuration as a function of the inertial number I. (a) heap height (h) normalized by the grain diameter (d); (b) h normalized by the filling height (H_0); (c) heap width (b) normalized by shear band width (W); and (d) heap middle point location (r_h) normalized by the shear band middle location (r_c). Hollow markers indicate tests where instabilities were observed. The dashed lines provide indications for characteristic ratios.

heaps with a width b below $2W$, while wider heaps are consistently observed in flows in the wall-collapsed regime [see Fig. 8(c)]. Similarly, the heap middle radial location r_h is in all cases greater than the shear band location r_c [see Fig. 8(d)], indicating that a small portion of the grains that conforms the heap are moving.

In other words, these observations point to a relation between the shear band within the granular material and its
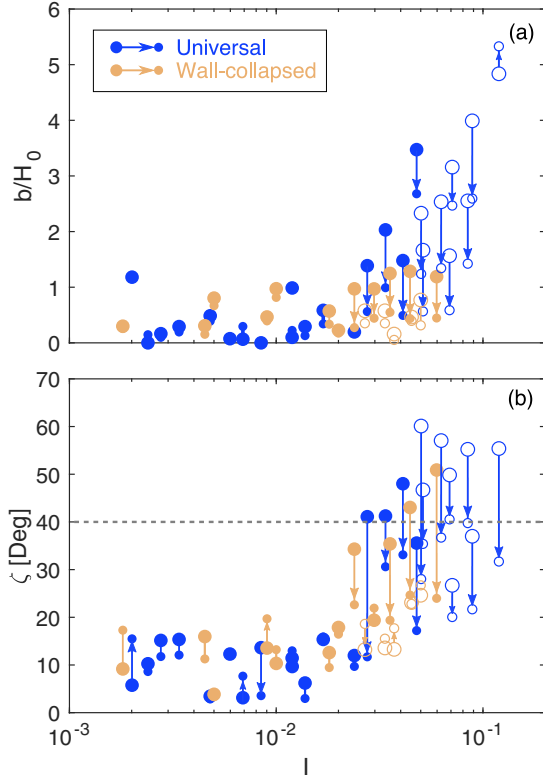
FIG. 9. Change of (a) heap width b and (b) heap inner slope ζ during shear (big markers) and after halt (small markers). The arrow indicates the change from continuous shear to halt, and the hollow markers indicate the observed instabilities. The horizontal dashed line in (b) marks the measured sand friction angle.

reflection on the heap formation. At low confining pressures, low filling heights, the shear band does not interact with the inner rotating cylinder, leading to lower and narrower heaps closer to r_c and located outer than R_s. At high confining pressures, high filling heights, the convection cell reorganizes, resulting in a new heap position radially inwards, but separates from r_c, while reducing the moving portion within the heap and increasing the amount of material that piles up.

After 100 rotations, shear is smoothly reduced until the cell comes to a halt. This deceleration results in a partial collapse of the heap [see Fig. 3(a)]. The heap collapse is characterized by a minimal decrease on its peak height and an inwards spread. The source of this collapse can be interpreted as the loss of the shear induced dilation and shear strength gained by the grains angularity. This loss leads to a reorganization of the granular structure within the now inactive convection cell [38,39].

The change on the heap morphology after halt can be measured as the change of the heap width b and the change of its inner slope ζ. Figure 9 presents these changes as a function of I, indicating with an arrow the transition from shear to halt. Changes in b and ζ amplify by increasing $\omega > 4.21$ rad/s ($\sim I > 0.02$), indicating a greater collective loss as the flow inertia is larger. Overall, both b and ζ decrease after stop, widening and flattening the heap.

As expected, the heap slope can be understood as a macroscopic representation of the granular internal friction angle, being $\zeta > 40°$ only for experiments in the highly inertial regime and of low confinement and $\zeta < 40°$ for all tests after halt. The variation of ζ can be linked to the heap height h, where the maximum values of h coincide with the maximum values of ζ.

The formation of heaps in sand flows reveal the need for accounting for this deformable free-surface condition in the numerical modeling of angular or slender grain flows in a split-bottom cell [18,37]. Moreover, these observations are relevant for the study of levees in natural flows down an unconfined inclined plane or when flowing along a curved path. In this configuration, a mixture of soil and large boulders form static regions between a flowing middle region [25,27,40]. These levees share the same height as the flowing material and provide a self-channelization that increases its final runout. After the flow is over, the levee height does not vary significantly, and as observed on the heaps, a side collapse lowers its slope.

B. Flow instabilities

The extended range of angular velocities explored in this series of experiments allows for the observation of two types of instabilities that interrupt the continuous flow within the cell. First, at high inertial flows ($I > 0.05$) and low confining pressures $H_0/d < 20$ mm, a macroscopic instability appears as the moving region displaces radially outwards and detaches from the rotating inner cylinder ($r_i > R_i$). Second, at high confining pressures, a localized instability is observed, where single grains on the surface are ejected when in contact with the rotating inner cylinder. Both types of instabilities widen the heap, by displacing the convective flow and translating more grains towards this region (see hollow markers in Fig. 9).

A previous study on fast rotating cells reported the transition from convex to concave height profiles in fast dense flows, highlighting the dependence of the convective cell speed with the width and radius of the moving annulus [29]. We observe a similar process in the high inertial flows and under low confining pressures. This instability can be
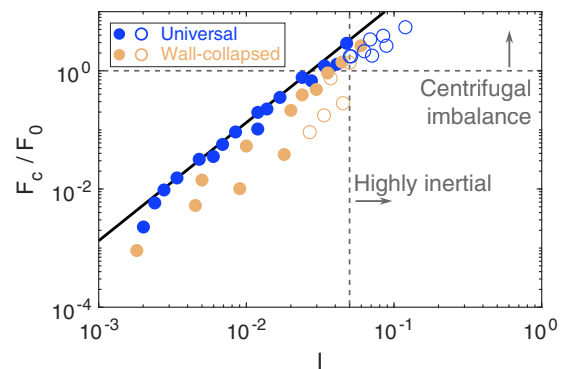

FIG. 10. The transition towards radial spreading is the result of the combination of a centrifugal imbalance ($F_c/F_0 > 1$) and highly inertial flows ($I > 0.05$). The continuous line corresponds to the prediction of Eq. (4), assuming $r_c = R_s$ and $r_i = R_i$.

described from the equilibrium in the moving annulus between the confining force ($F_0 \propto \rho g H_0$) and the centrifugal force ($F_c \propto \rho \omega^2 R_s$). The cross section of the moving annulus can be simplified by a rectangle of height H_0 and width ($r_c - r_i$), where H_0 and r_c are parameters from the initial configuration and shear band, respectively. The equilibrium at the moving annulus can be written as

$$\frac{F_c}{F_0} = \frac{\omega^2 R_s (r_c - r_i)}{g H_0} = I^2 R_s \left(\frac{r_c - r_i}{d^2} \right). \qquad (4)$$

A ratio of $F_c/F_0 > 1$ would lead to a centrifugal imbalance. Under this imbalance the induced centrifugal force overcomes the self-weight and changes the pressure gradient within the granular medium. However, for the instability to appear, higher levels of inertia are required (see Fig. 10). This level is reached in our experiments at $I > 0.05$, and can be related with a higher level of agitation within the moving annulus.

An understanding of these dynamics, may provide the theoretical foundations on the kinematics of mass flows with superelevation and levee formation [41].

Ejected particles are exclusive to flows within the wall-collapsed regime. In this regime, the shear band is in contact with the inner cylinder and the surface velocity profile has its maximum at $r = R_i$. An explanation for this instability results from the dilation within the shear band that eases the lateral confinement within the moving grains. The reduced confinement allows the grains to be suddenly impulsed by the rotating cylinder. Note that in the wall-collapsed regime, the moving annulus is slower than the rotating cylinder ($u_\theta < \omega R_i$). The interaction between the grains and the rotating cylinder results in a continuous ejection of particles, widening and flattening the heap (see Fig. 9). Moreover, the amount and reach of the ejected grains is amplified by an increase in ω. A detailed study of the mechanism behind particle ejection is outside the scope of this work, but it could provide a valuable insight into the transition from dense to dilute granular flows.

The physics behind the occurrence of radial spread or particle ejection are directly linked to the competing forces driven by gravity and the cylinder rotation in a split-bottom cell. This competition is clearly represented by I and cannot be treated separately as shown in Fig. 6. A significantly larger system may abate the relation between the instabilities and the heap dimensions, by distancing the location of r_c, but its occurrence will not vanish. These limit processes may serve as a reference scenario for developing more efficient mixing methods or may provide a deeper understanding of natural mass flows, considering a wider spectrum of granular flow regimes.

V. CONCLUSIONS

In this work, we studied the flow of angular grains in a split-bottom Couette cell, extending the observations towards highly inertial flows and complementing the collection of behaviours in this shear configuration. We examined the heaps formed during shear, while exploring the transition from slow to moderately highly inertial flows. The role of angularity is key in the formation of the heap, being independent of the flow regimes within the cell and agreeing with the known grain

shape effects in split-bottom cells. The flow regimes agree with previous observations in split-bottom cells, pointing to an intrinsic relation with the Froude number in the moving annulus. Moreover, the location of the shear band within the granular medium is found to be dependent to the applied shear rate in moderately high inertial flows ($I \geqslant 10^{-2}$), moving inwards under low filling heights. The internal mechanisms leading to the displacement of the shear towards the cell center band at moderately high inertial flows remains to be clarified.

The heap morphology is found to be amplified by increasing the flow inertia, resulting in higher and wider heaps. The heap morphology is linked with the shear band within the granular medium, and is found to be controlled by the confinement provided by the medium self-weight. Once the cell starts to decelerate, part of the heap collapses, resulting in slightly shallower and flatter heaps. This change in heap morphology is acknowledged to result from the loss of dilation gained by shape effects, moving the granular medium to a static equilibrium after halt. Finally, the observed instabilities result from the imbalance caused by an increase in the centrifugal acceleration within the moving annulus. At low confinement, the whole moving region spreads radially outwards; while at high confinement, the localized interaction of grains with a faster rotating wall results in particle ejections. These instabilities set an interesting point for the study of flows transitioning from dense to dilute granular flows. Based on the insights presented in this work, further efforts in modeling the rheology of granular media in split-bottom cells should consider the alteration of its free surface. Future studies might also focus on exploring the ranges of sphericity and roundness combinations, evaluating their influence on the heap formation. An understanding of such features can result in interesting repercussions on the simulation of grain shape effects on geophysical mass flows.

APPENDIX: DATA SUMMARY

In this Appendix we provide in Table I a detailed summary of the experimental data during shear for experiments with sand. The quantities here reported are the cell filling height (H_0), cell angular velocity (ω), shear band radial center (r_c), shear band width (W), heap height (h), heap width (b), heap radial center (r_h), tangential component of the flow velocity (u_θ), radial component of flow velocity (u_r), heap slope (ζ), and the innermost radial location of the granular medium (r_i). For more details on these quantities, refer to Secs. III and IV.

TABLE I. Summary of shear band and heap measurements during shear in sand.

H_0 [mm]	ω [rad/s]	r_c [mm]	W [mm]	h [mm]	b [mm]	r_h [mm]	u_θ [m/s]	u_r [m/s]	ζ [deg]	r_i [mm]
10	0.85	106.26	16.09	2.68	4.86	121.00	0.08	0.00	3.45	65.00
10	2.11	106.30	14.96	3.40	9.86	121.80	0.20	0.00	9.68	65.00
10	4.23	105.32	5.49	1.97	1.96	127.10	0.40	0.00	11.98	65.00
10	8.45	103.11	8.33	5.80	34.73	118.66	0.75	0.00	35.56	65.00
10	12.57	98.91	7.76	9.83	31.59	122.88	0.94	−0.01	26.7	86.43
10	15.71	102.94	6.10	9.55	39.9	120.75	0.77	−0.04	36.99	91.19
10	21.12	104.31	4.86	11.60	48.36	117.64	0.79	−0.06	55.39	92.91
20	0.85	104.95	13.59	2.93	5.85	118.18	0.08	0.00	15.36	65.00
20	2.11	103.53	8.16	1.66	0.00	118.91	0.19	0.00	13.63	65.00
20	4.23	102.08	7.69	4.55	11.69	117.58	0.37	0.00	15.36	65.00
20	8.45	96.61	10.55	7.93	40.62	111.91	0.68	−0.01	41.24	65.00
20	12.57	90.59	15.88	12.81	46.60	110.22	0.89	−0.03	60.10	69.76
20	15.71	95.86	10.53	13.03	50.71	112.14	0.82	−0.06	57.05	79.63
20	21.12	95.29	9.55	14.24	51.04	114.24	0.85	−0.07	55.23	78.95
30	0.85	102.46	13.85	2.00	4.94	116.24	0.07	0.00	15.15	65.00
30	2.11	100.55	9.25	2.57	1.97	111.62	0.18	0.00	3.13	65.00
30	4.23	100.42	13.00	3.04	8.74	120.12	0.34	0.00	6.22	65.00
30	8.45	91.59	15.39	5.49	41.61	105.92	0.60	−0.01	41.09	65.00
30	12.57	87.85	15.74	7.49	44.36	108.56	0.80	−0.04	48.01	65.00
30	15.71	89.75	12.76	9.02	49.96	108.74	0.79	−0.06	46.71	67.44
30	21.12	91.18	11.08	9.21	46.98	108.33	0.76	−0.11	49.85	69.88
40	0.85	95.18	11.42	1.61	0.00	135.25	0.06	0.00	10.25	65.00
40	2.11	94.61	10.61	2.71	2.98	117.47	0.16	0.00	12.29	65.00
40	4.23	86.65	14.34	2.91	3.97	121.47	0.31	0.00	11.46	65.00
40	8.45	85.47	14.76	5.15	38.85	104.39	0.53	0.00	34.29	65.00
40	12.57	86.71	13.61	7.56	49.91	106.47	0.64	−0.02	35.40	65.00
40	15.71	86.21	12.82	9.14	51.41	106.39	0.66	−0.08	43.03	65.00
40	21.12	87.22	10.27	7.91	47.61	105.77	0.66	−0.11	50.89	65.00
57	0.85	81.83	12.15	6.83	67.31	95.95	0.05	0.00	5.76	65.00
57	2.11	81.87	12.10	5.77	45.85	94.87	0.12	0.00	3.85	65.00
57	4.23	80.89	10.93	7.07	55.46	95.79	0.20	0.00	10.33	65.00
57	8.45	80.96	10.69	4.38	12.93	116.18	0.32	−0.01	17.86	65.00
57	12.57	81.24	9.26	6.60	55.27	99.70	0.37	−0.02	19.39	65.00
57	15.71	81.12	9.01	3.90	8.99	116.47	0.41	−0.01	13.28	65.00
57	21.12	81.35	10.47	6.84	43.89	107.26	0.48	−0.01	24.62	65.00
70	0.85	73.26	4.46	3.85	20.96	106.46	0.02	0.00	9.17	65.00
70	2.11	72.69	7.38	4.98	21.50	106.75	0.07	−0.01	15.96	65.00
70	4.23	68.71	9.15	6.68	32.56	109.17	0.12	−0.01	13.55	65.00
70	8.45	68.51	9.81	6.97	40.00	99.65	0.21	−0.01	12.60	65.00
70	12.57	68.79	9.18	7.21	40.33	102.36	0.25	−0.01	13.21	65.00
70	15.71	69.67	8.44	7.21	40.33	102.36	0.29	−0.01	13.58	65.00
70	21.12	69.14	7.15	6.26	32.56	109.17	0.24	−0.01	23.09	65.00

[1] S. Courrech du Pont, P. Gondret, B. Perrin, and M. Rabaud, Granular Avalanches in Fluids, Phys. Rev. Lett. **90**, 044301 (2003).

[2] E. Azéma, N. Estrada, and F. Radjai, Nonlinear effects of particle shape angularity in sheared granular media, Phys. Rev. E **86**, 041301 (2012).

[3] J. M. N. T. Gray, Particle segregation in dense granular flows, Annu. Rev. Fluid Mech. **50**, 407 (2018).

[4] K. van der Vaart, A. Thornton, C. Johnson, T. Weinhart, L. Jing, P. Gajjar, J. Gray, and C. Ancey, Breaking size-segregation waves and mobility feedback in dense granular avalanches, Granular Matter **20**, 46 (2018).

[5] A. Leonardi, M. Cabrera, F. K. Wittel, R. Kaitna, M. Mendoza, W. Wu, and H. J. Herrmann, Granular-front formation in free-surface flow of concentrated suspensions, Phys. Rev. E **92**, 052204 (2015).

[6] M. Cabrera and N. Estrada, Granular column collapse: Analysis of grain-size effects, Phys. Rev. E **99**, 012905 (2019).

[7] D. M. Wood, *Soil Behavior and Critical State Soil Mechanics* (Cambridge University Press, Cambridge, 1990).

[8] L. Rondon, O. Pouliquen, and P. Aussillous, Granular collapse in a fluid: Role of the initial volume fraction, Phys. Fluids **23**, 073301 (2011).

[9] G. MiDi, On dense granular flows, Eur. Phys. J. E **14**, 341 (2004).

[10] H.-B. Mühlhaus and I. Vardoulakis, The thickness of shear bands in granular materials, Geotechnique **37**, 271 (1987).

[11] K. A. Reddy, Y. Forterre, and O. Pouliquen, Evidence of Mechanically Activated Processes in Slow Granular Flows, Phys. Rev. Lett. **106**, 108301 (2011).

[12] P. Schall and M. van Hecke, Shear bands in matter with granularity, Annu. Rev. Fluid Mech. **42**, 67 (2010).

[13] D. Fenistein and M. van Hecke, Wide shear zones in granular bulk flow, Nature (London) **425**, 256 (2003).

[14] D. Fenistein, J. W. van de Meent, and M. van Hecke, Universal and Wide Shear Zones in Granular Bulk Flow, Phys. Rev. Lett. **92**, 094301 (2004).

[15] R. Mikkelsen, Granular dynamics: Clustering and shear flows, Ph.D. thesis, University of Twente, the Netherlands (2005).

[16] S. Wegner, R. Stannarius, A. Boese, G. Rose, B. Szabo, E. Somfai, and T. Börzsönyi, Effects of grain shape on packing and dilatancy of sheared granular materials, Soft Matter **10**, 5157 (2014).

[17] S. Roy, S. Luding, and T. Weinhart, A general (ized) local rheology for wet granular materials, New J. Phys. **19**, 043014 (2017).

[18] D. L. Henann and K. Kamrin, A predictive, size-dependent continuum model for dense granular flows, Proc. Natl. Acad. Sci. USA **110**, 6730 (2013).

[19] S. Roy, B. J. Scheper, H. Polman, A. R. Thornton, D. R. Tunuguntla, S. Luding, and T. Weinhart, Surface flow profiles for dry and wet granular materials by particle tracking velocimetry; the effect of wall roughness, Eur. Phys. J. E **42**, 14 (2019).

[20] R. D. Hryciw, J. Zheng, and K. Shetler, Particle roundness and sphericity from images of assemblies by chart estimates and computer methods, J. Geotech. Geoenviron. Eng. **142**, 04016038 (2016).

[21] G. Wortel, T. Börzsönyi, E. Somfai, S. Wegner, B. Szabó, R. Stannarius, and M. Van Hecke, Heaping, secondary flows and broken symmetry in flows of elongated granular particles, Soft Matter **11**, 2570 (2015).

[22] D. Fischer, T. Börzsönyi, D. S. Nasato, T. Pöschel, and R. Stannarius, Heaping and secondary flows in sheared granular materials, New J. Phys. **18**, 113006 (2016).

[23] E. Azéma, F. Radjai, and F. Dubois, Packings of irregular polyhedral particles: Strength, structure, and effects of angularity, Phys. Rev. E **87**, 062203 (2013).

[24] A. Mangeney, F. Bouchut, N. Thomas, J. P. Vilotte, and M. Bristeau, Numerical modeling of self-channeling granular flows

and of their levee-channel deposits, J. Geophys. Res. **112**, 1 (2007).

[25] C. Johnson, B. Kokelaar, R. Iverson, M. Logan, R. LaHusen, and J. Gray, Grain-size segregation and levee formation in geophysical mass flows, J. Geophys. Res. **117**, 1 (2012).

[26] B. Kokelaar, R. Graham, J. Gray, and J. W. Vallance, Fine-grained linings of leveed channels facilitate runout of granular flows, Earth Planet. Sci. Lett. **385**, 172 (2014).

[27] F. Rocha, C. Johnson, and J. Gray, Self-channelisation and levee formation in monodisperse granular flows, J. Fluid Mech. **876**, 591 (2019).

[28] T. T. Vo, S. Nezamabadi, P. Mutabaruka, J.-Y. Delenne, and F. Radjai, Additive rheology of complex granular flows, Nat. Commun. **11**, 1 (2020).

[29] E. I. Corwin, Granular flow in a rapidly rotated system with fixed walls, Phys. Rev. E **77**, 031308 (2008).

[30] J. Zheng and R. D. Hryciw, Traditional soil particle sphericity, roundness and surface roughness by computational geometry, Géotechnique **65**, 494 (2015).

[31] J. Zheng and R. D. Hryciw, Roundness and sphericity of soil particles in assemblies by computational geometry, J. Comput. Civ. Eng. **30**, 04016021 (2016).

[32] R. Cox, W. A. Lopes, and K. L. Jahn, Quantitative roundness analysis of coastal boulder deposits, Mar. Geol. **396**, 114 (2018).

[33] J. L. Anthony and C. Marone, Influence of particle characteristics on granular friction, J. Geophys. Res. **110**, 1 (2005).

[34] W. Thielicke and E. J. Stamhuis, PIVlab–Towards user-friendly, affordable and accurate digital particle image velocimetry in MATLAB, J. Open Res. Softw. **2**, e30 (2014).

[35] J. A. Dijksman and M. van Hecke, Granular flows in split-bottom geometries, Soft Matter **6**, 2901 (2010).

[36] T. Unger, J. Török, J. Kertész, and D. E. Wolf, Shear Band Formation in Granular Media as a Variational Problem, Phys. Rev. Lett. **92**, 214301 (2004).

[37] P. Jop, Hydrodynamic modeling of granular flows in a modified Couette cell, Phys. Rev. E **77**, 032301 (2008).

[38] Y. Fan and K. M. Hill, Shear-driven segregation of dense granular mixtures in a split-bottom cell, Phys. Rev. E **81**, 041303 (2010).

[39] K. Krishnaraj and P. R. Nott, A dilation-driven vortex flow in sheared granular materials explains a rheometric anomaly, Nat. Commun. **7**, 10630 (2016).

[40] S. P. Pudasaini and K. Hutter, Rapid shear flows of dry granular masses down curved and twisted channels, J. Fluid Mech. **495**, 193 (2003).

[41] C. Scheidl, B. W. McArdell, and D. Rickenmann, Debris-flow velocities and superelevation in a curved laboratory channel, Can. Geotech. J. **52**, 305 (2015).